Critical dynamic vortex fluctuations amidst a nascent peak effect in granular CeRu$_2$ films

Critical dynamic vortex fluctuations amidst a nascent peak effect in granular CeRu$_2$ films

B J Taylor, R E Baumbach, T A Sayles and M B Maple

Department of Physics and Institute for Pure and Applied Physical Sciences, University of California, San Diego, La Jolla, CA 92093, USA

Abstract
A peak effect has been investigated in granular CeRu$_2$ films, grown via the method of pulsed laser deposition. The films exhibit residual resistivities and low field pinning force densities comparable to those for single crystals, yet the peak effect is not readily observable in electrical resistivity, $\rho(H, T)$, or magnetization, $M(H)$, measurements. The emergence of an increase in pinning force density corresponding to the known region of the peak effect is observed in films with larger grain size ($d \sim 10 \ \mu$m). Furthermore, in the large grain size films, within the region of enhanced pinning, scaling properties of voltage–current, V–I, data indicate a suppression of the superfluid density with a maximum corresponding to the pinning force peak. This phenomenon is seen to correspond to an anomalous feature found by Yoshizawa *et al* (1997 *J. Phys. Soc. Japan* **66** 2355) in the transverse elastic moduli $(c_{11} - c_{12})/2$ of single crystals, and to anomalous magnetostriction effects observed by Tachiki *et al* (1996 *Z. Phys.* B **100** 369), and is consistent with an anomalous enhancement of the magnetic penetration depth observed by Yamashita *et al* (1997 *Phys. Rev. Lett.* **79** 3771). A conventional explanation of the peak effect in CeRu$_2$ based upon structural/electronic fluctuations is proposed. Additional evidence indicates that the enhanced ability of the vortices to couple to the atomic lattice, made possible by the softness of the transverse atomic moduli, *and* the collective critical behavior of the vortices, may also play an important role in the peak effect mechanism.

1. Introduction

The exotic superconducting compound CeRu$_2$, discovered in 1958 by Matthias *et al* [1] is a well known and heavily studied material. The past decade has seen intense renewed interest in this material due to it having some basic similarities to both high-T_c cuprate and heavy-fermion superconductors, and also due to the observation of the so called 'peak effect', an anomalous mixed state behavior wherein the vortex ensemble undergoes a transition to a considerably stronger pinning configuration resulting in a large increase of the critical current density within in a region near to the upper critical field, $H_{c2}(T)$. Various mechanisms have been proposed for the origin of the peak effect in CeRu$_2$. One possibility that has been revisited is the inhomogeneous generalized Fulde–Ferrel–Larkin–Ovchinnikov (GFFLO) superconducting state [2, 3] which has a spatially modulated order parameter along the magnetic field direction [4]. Despite the extensive number

of studies devoted to understanding the nature of the peak, and the large volume of evidence against the FFLO state, debate still persists as to whether or not it exists in CeRu$_2$, and is thus responsible for the peak effect in this compound. A more conventional explanation of the peak effect involves the collective bundle pinning scenario with a high density of weak pinning cites leading to a dynamical two-step depinning process [5]. The focus of other studies has been on the role of the few strong point defects and the possibility of unconventional pinning forces arising as a result of the renormalized electronic state due to valence fluctuations [6].

A number of studies strongly suggest that the structural properties of the crystal play a significant, perhaps essential, role in the mechanism of the peak effect.

(i) Ultrasound measurements have shown a substantial softening ($\sim$50%) of the shear modulus of CeRu$_2$ from room temperature down to $\sim$20 K with a small upturn down to $\sim$6 K without a structural phase transition taking

place, pointing to the persistence of strong structural fluctuations [7]. At $T = T_c \sim 6$ K in zero field, further softening is observed by an anomalous downward kink in the shear moduli, which is suppressed to lower temperatures by application of a magnetic field. Upon closer examination of the region of the kink, further anomalous hysteretic field/temperature behavior of the shear modulus was seen [8]. We observe here that this latter behavior is correlated with various hysteretic properties of the peak effect, including hysteresis in magnetization, $M(H)$, for minor magnetic field loops [9], and distinct regions of the magnetization $M(H)$ loop exhibiting differing relaxation rates [10].

(ii) It has been observed that the peak effect can be destroyed in single crystal samples by a rapid cooling of the sample from room temperature to ∼6 K [10]. This is consistent with the peak effect being tied to the softening of the atomic lattice moduli. By rapidly cooling the sample, it is work hardened, removing the necessary softness of the crystal for the peak effect.

(iii) Magnetostriction measurements, $\Delta \ell(H)$, in the peak effect region revealed an anomalous *increase* in the length of the crystal along the direction of the applied magnetic field [4]. This behavior was also seen to be hysteretic as a function of field, and is readily seen to be associated with the peak effect. Even if the conclusion that the unusual field dependent behavior of the magnetostriction is evidence for the FFLO state is not correct, the correlation between $\Delta \ell(H)$ and the peak effect remains.

A common characteristic of the peak effect observed in various systems is that it only occurs in pure materials that contain extremely weak pinning forces, and as such is only observed in high quality single crystals. We have successfully grown films of $CeRu_2$ with pinning force densities *weaker* than that seen in some single crystals. In a effort to further understand the peak effect mechanism in $CeRu_2$ we have grown thick film samples and have investigated their peak effect properties via electrical transport, $\rho(H,T)$, critical current density, $J_c(H,T)$, and magnetization, $M(H,T)$, measurements. Previous efforts by Groten *et al* [11] to make $CeRu_2$ films resulted in samples with pinning force densities so strong that the region of peak effect, where enhanced pinning takes place, was effectively buried beneath the strong defect pinning. The films in this study fall into a small grain ($d_{max} \sim 2$ μm) or large grain (island) ($d_{max} \sim 10$ μm) category, and exhibit significantly different transport properties which are thought to give insight as to the nature of the peak effect mechanism. The films exhibit residual resistivities comparable to moderate quality single crystals, and yet exhibit pinning force densities, $F_p(H,T)$, *less than* that found in high quality single crystals, and as such are expected to exhibit peak effect behavior. Remarkably though, the peak effect is missing in these samples from both transport, $\rho(H,T)$, and magnetization, $M(H)$, measurements. This is *not* due to strong disorder pinning overriding the peak effect region, as seen in the previous study of $CeRu_2$ films [11].

In this paper, we present evidence based on the above measurements for a suppression of the superfluid density, ρ_s,

in the region of the peak effect, the maximum of which is centered at the maximum of the magnetization hysteresis loop. This observation of a suppression of the superfluid density is consistent with results from μSR measurements of the magnetic penetration depth, λ [12, 13], wherein an anomalous increase of λ was found in the peak effect region, and as such indicates a corresponding increase of normal state electrons, quasiparticles, outside the vortex cores. These results are consistent with the existence of a nodal vortex state, i.e., the FFLO state. However, we consider the possibility that there is a more conventional explanation for the increase of quasiparticles related to the well known structural fluctuations. Furthermore, we observe that the critical behavior of the vortices may also play an important role in the peak effect mechanism through an enhancement of the coupling of the vortices to the underlying fluctuating atomic/electronic host.

2. Experimental details

Thick films of $CeRu_2$ were synthesized by pulsed laser deposition (PLD) using a Lambda Physik KrF laser with a wavelength of 248 nm. A polycrystalline $CeRu_2$ boule was prepared for use as an ablation target by arc-melting a stoichiometric mixture of Ce and Ru under an inert Ar atmosphere near 1 atm based on the procedure described by Dilley *et al* [5]. During the process, extra Ce was added to compensate for the Ce loss that occurs during arc-melting. The boule was then cut using a diamond wheel saw and was subsequently polished to yield a smooth surface. The resulting target had a 1.5 cm diameter surface and a thickness of 0.5 cm. Ablation took place in a clean background of $\sim 1 \times 10^{-5}$ Torr UHP Ar after initially pumping down to a base pressure of $\sim 5 \times 10^{-10}$ Torr. Films ranging in thickness from 1000 Å– 4.5 μm were grown on r-plane cuts of sapphire (Al_2O_3) (films 'A' and 'B',) and on c-plane cuts of lanthanum aluminate ($LaAlO_3$) (film 'C'). The thickness of samples presented in this study are 4 μm (film 'A') and 4.5 μm (films 'B' and 'C'), with planar dimensions of $\sim 1 \times 2$ cm^2. The target to substrate distance was 3.2 cm, and the estimated energy density of the beam on the target was ~ 5 J cm^{-2} for film 'A' and ~ 20 J cm^{-2} for 'B' and 'C'. Films were found to grow best at 400 °C. Growth was followed by an *in situ* anneal at 760 °C for 30 min.

Magnetization $M(T)$ and $M(H)$ data were taken using a Quantum Design Magnetic Property Measurement System (MPMS) in fields up to 5.0 T and for temperatures from 1.8 K up to 10 K. For magnetotransport measurements, gold leads were attached with silver epoxy to gold pads sputtered on the films, with the resulting contact resistance <1 Ω. Standard four-wire DC resistance measurements were performed using a Keithley 220 current source, a Keithley 2182 nanovoltmeter, and a Quantum Design Physical Property Measurement System (PPMS) from temperatures 1.8 to 300 K and in fields up to 9.0 T. Electrical resistivity, $\rho(H,T)$ measurements were made in a static manner, that is, at incremental values of the magnetic field (temperature) for a given fixed temperature (field). Unless otherwise stated, all resistivity data were taken by preparing the sample in a zero field cooled (ZFC) initial state. Then, for $\rho(T)$ data, a field was applied, followed
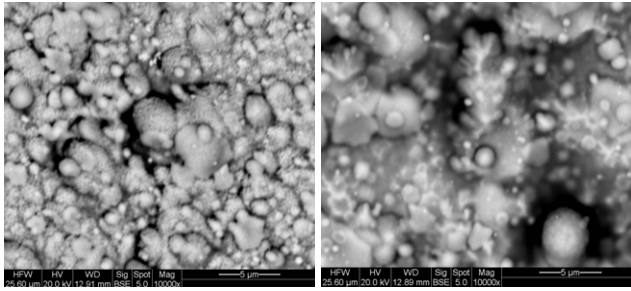
Figure 1. SEM image of CeRu$_2$ films 'A' (SG) (left) and 'B' (LG) (right) grown on Al$_2$O$_3$ substrates (*r*-plane cut). The films were grown under identical conditions (see the text) with the exception of the laser ablation energy density. The energy densities were $\sim$5 J cm^{-2} and $\sim$20 J cm^{-2} for the small and large grain films, respectively. Both films are well into the clean limit with mean paths within the grains $\ell \sim$ 1000–2000 Å.

by incremental increases of temperature to a maximum a few degrees above T_c, then lowered by the same increments. Following the ZFC to a fixed temperature, $\rho(H)$ data were taken in incremental increasing field steps to a maximum of 7–9 T, then lowered by the same increments. A sample was also cut from the target material for comparison of magnetization and electrical transport properties. It was polished to have sample dimensions $\ell \times w \times t = 0.245$ cm $\times$ 0.111 cm $\times$ 33 μm. The thickness is $\sim$8 times that of the films. The magnetic field for all of the above measurements was applied perpendicular to the film surface and to the largest target sample surface.

3. Experimental results

Films grown on LaAlO$_3$ substrates were found to have very high pinning force densities which overwhelmed the peak effect region. These films were grown at the same time as those on Al$_2$O$_3$ substrates. The main results examined in this study are the low pinning force density films grown on Al$_2$O$_3$ substrates. We present results from the films grown on LaAlO$_3$ to demonstrate that the unusually low pinning force density is intrinsic to the Al$_2$O$_3$ grown films. The morphology of the small grain (SG) film 'A' is primarily granular with some island type growth. In the large grain (LG) film 'B', the predominant structures are islands of diameter $d \approx 10$ μm which appear to be partially in direct contact with each other, with smaller grains in the open regions between and on the surface. X-ray diffraction data shown in figure 2, demonstrate that the films are polycrystalline and the island growth is primarily aligned along the $\langle 111 \rangle$ direction. Some minor impurity phases of Ce–Ru intermetallics are also seen. The SEM data (figure 1) show that the surface of the films and the regions between the islands are granular with grain diameters (along the *a*–*b* plane of the substrate) ranging in size from $d \sim$ 0.5–2 μm for film 'A' and $d \sim$ 1–5 μm for film 'B'. The higher intensities of the x-ray diffraction data for film 'B' over that of 'A' is readily attributable to the larger average grain size of the film.

The superconducting magnetic transitions, $\chi \equiv 4\pi M(T)/H$, of the target sample and the two films are shown in figure 3. The value of the onset critical temperature, T_c^{onset}, is
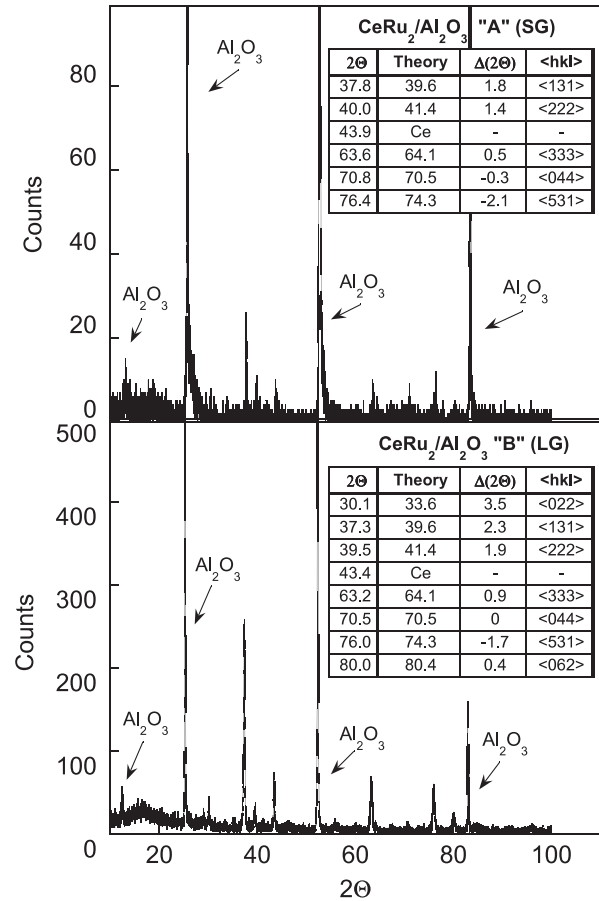

Figure 2. X-ray diffraction data for the small grain film, 'A' (top panel), and the large grain film 'B' (bottom panel). The difference in average grain size is evident by the increase of count number. The primary crystalline alignment is along the $\langle 111 \rangle$ direction. Other orientations are also present along with minor Ce–Ru impurity phases.

6.2 and 5.7 K, with 10%–90% transition widths, $\Delta T_c \approx 0.64$ and 0.45 K for the target and films, respectively. The target sample exhibits a full Meissner effect, within experimental error, demonstrating the quality of the target material. The insets to figure 3 show $\chi \equiv 4\pi M/H$ data of the films. The magnetization data in inset (a) was adjusted by accounting for an effective enhancement of the superconducting volume due to the coating of the edges of the substrate with CeRu$_2$. The effect of the substrate edges being coated with CeRu$_2$ is to shield the magnetic field over a greater volume than just that of the film dimensions. The edge coating is not uniform and does not extend over the entire thickness of the substrate. While it is difficult to estimate to what extent the edge coating affects the magnetization measurement, the thickness of the effective volume, $t = t_{\text{film}} + (x\%)t_{\text{substrate}}$ is found by assuming a full Meissner effect and solving for the additional thickness needed after accounting for a demagnetization factor [14].

Resistivity data from the two films and from a sample taken from the PLD target material are shown in figure 4. The resistivities, $\rho(T)$, of all three samples are qualitatively similar. However, film 'B' shows signs of substrate–film interface strain as a result of mismatched thermal expansion
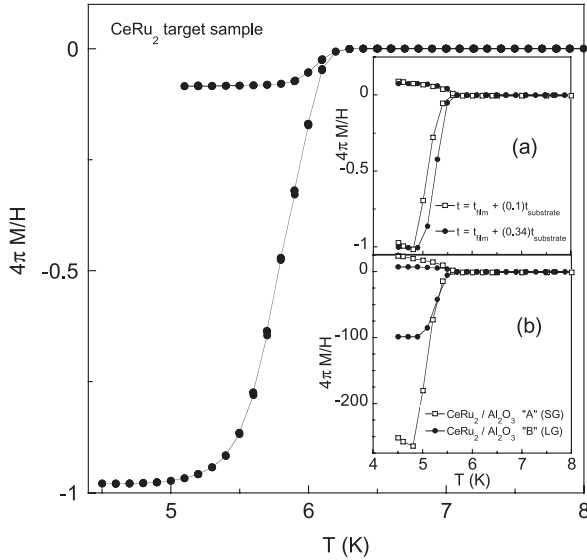
Figure 3. Magnetic susceptibility, $\chi \equiv 4\pi\, M/H$, data for the target sample and films (inset). Inset (a) shows adjusted values of χ for the films after taking into account an effective volume due to the coating of the substrate edges with superconducting material. Inset (b) shows the unphysically large values of χ for the films found by using the film dimensions. See the text for details.

Figure 4. Resistivity, $\rho(T)$, data for target sample and films 'A' and 'B'. Note that the larger grain size (more crystalline) film, 'B', shows signs of substrate–film interface strain upon cooling: the intrinsic residual resistivity of 'B' is estimated to be a factor of 2 smaller than shown.

rates. This is naturally of more importance in the large grain (LG) crystalline film, since the sizes of the grains of the LG film are equal to or greater than the film thickness resulting in the majority of the grains being connected to the substrate surface. The largest grains of the small grain (SG) film are approximately equal to or less than the film thickness. The critical temperature, defined as the midpoint of the resistive transition, is $T_c = 6.1$ K for the target sample, and $T_c = 6.0$ K for both of the films, with ΔT_c defined as the 10%–90% resistivity values, $\Delta T_c \approx 0.2$ K and 0.3 K for the target and films respectively. The residual resistivities are $\rho_0 \approx 15\ \mu\Omega$ cm and $\rho_0 \approx 30\ \mu\Omega$ cm, for the target sample and the films (inset figure 4). The residual resistivity of film 'B' is estimated to be approximately a factor of two less than that shown without the effect of the substrate strain. The electronic mean free path, ℓ, in the films was estimated by comparison of the residual resistivities of the films to that of a single crystal whose mean free path was determined by de Haas–van Alphen measurements [15] where $\rho_0 = 0.6\ \mu\Omega$ cm, $\xi_0 = 79$ Å, the residual resistivity ratio is 270, and the mean free path is $\ell \approx 2000$–2400 Å, depending upon the field–crystal orientation.

From the relation $\rho_n \ell = [\frac{2}{3} N(0) v_F e^2]^{-1}$ we have $\ell_{\mathrm{film}} = \ell_{\mathrm{bulk}} \frac{\rho_{n(\mathrm{bulk})}}{\rho_{n(\mathrm{film})}}$. This gives $\ell_{\mathrm{film}} \approx 58$ Å. From the relation $\ell_{\mathrm{film}}/\ell_{\mathrm{bulk}} = RRR_{\mathrm{film}}/RRR_{\mathrm{bulk}}$ [5], where RRR is the residual resistivity ratio $\rho(300K)/\rho_0$, we find $\ell_{\mathrm{film}} \approx 35$ Å. Either estimate gives $\ell < \xi_0$ implying that the films are in the dirty regime, which is in conflict with the conclusion reached from the pinning force density measurements described below, where the pinning of vortices in the films is found to be similar to that found in high quality single crystals. This contradiction can be resolved by recognizing that it is likely that the connections between the grains and/or islands are
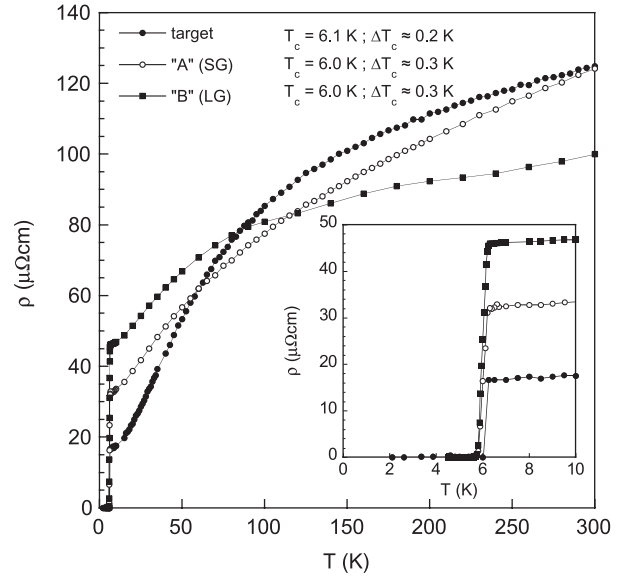
considerably more resistive than the crystal material due to the high resistivity of the junctions between grains. If instead, we make use of a property of very clean superconductors wherein the introduction of a small amount of point disorder, the upper critical field, $H_{c2}(0)$, will be enhanced as a result of the decrease of the superconducting coherence length ξ with minimal effect upon the critical temperature T_c [16], we arrive at the relation

$$\ell_{\mathrm{film}} = \ell_{\mathrm{bulk}} \left(\frac{\xi_{\mathrm{film}}(0)}{\xi_{\mathrm{bulk}}(0)} \right)^2. \qquad (1)$$

This gives $\ell_{\mathrm{film}} \approx 1800$ Å for the small grain film and $\ell_{\mathrm{film}} \approx 1600$ Å for the large grain film. It seems most likely that the crystalline grains of the films have a defect density and corresponding mean free path comparable to single crystals. If this is true, then the grains of the SG film, with diameters of $d \sim 0.1$–2 μm have few if any defects. The grains of the LG film, with diameters of $d \sim 0.5$–10 μm have only a small number of defects. The primary source of impedance to vortex motion in the SG films is the surface barrier of the grains and defects within any amorphous material between the grains. Further evidence for a very low density of defects within the SG sample is found from low current resistivity, $\rho(T)$, and V–I data. The natural log of the resistivity versus inverse temperature, $\ln(\rho(T))$ versus $1/T$, at various magnetic fields, is plotted in figure 5. The data conform to a thermally assisted flux flow (TAFF) type behavior over the linear portions as plotted, corresponding to a resistivity that is described by $\rho(T) = \rho_0 \exp[-U/k_B T]$ [8].

In contrast, the large grain film exhibits resistivity, $\rho(T)$, behavior suggestive of first order melting of a vortex lattice. In figure 6 and the inset, the sharpness of the resistive
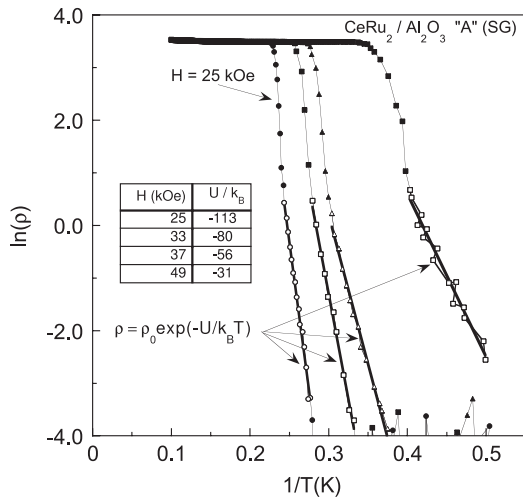
Figure 5. Natural log of the resistivity versus inverse temperature, $\ln \rho(T)$ versus $1/T$, data from film 'A'. The data demonstrate that the vortex ensemble is in a TAFF regime in this film.
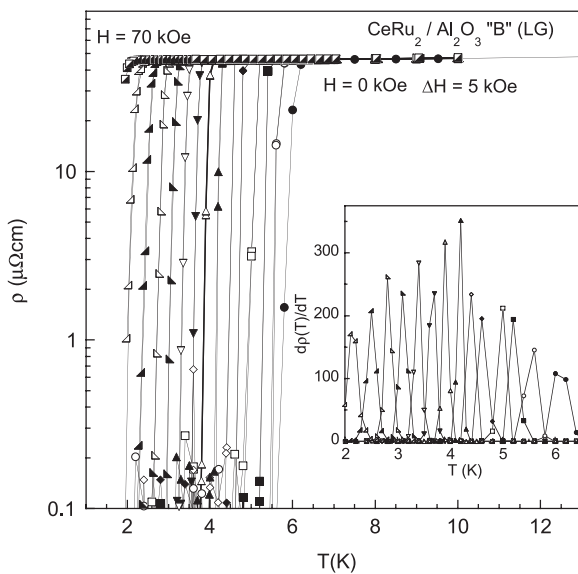

Figure 6. Resistivity, $\rho(T)$, data for film 'B'. Note that the peak effect like behavior seen in the $\rho(H)$ data is not observable here. The sharpness of the $\mathrm{d}\rho(T)/\mathrm{d}T$ data for film 'B' indicates that the melting transition is, or is very nearly, a first order vortex lattice melting transition. Transition widths do not broaden measurably with field, with $\Delta T \approx 0.2$ K for all fields.

Figure 7. Resistivity, $\rho(H)$, data for films 'A' and 'B'. The inset shows data from both samples at $T = 4.5$ K, normalized to ρ_0 and to the field value of the onset of the transition, for comparison of behavior in the region where the peak effect is usually observed. See the text for further discussion.

superconducting transition in various magnetic fields is seen in both $\rho(T)$ and $\mathrm{d}(\rho(T))/\mathrm{d}T$, with transition widths of $\Delta T \sim 0.2$ K for all fields. However, no measurable hysteresis in temperature could be observed, so the transition may just be a very clean vortex glass [17–19], or Bragg glass [20] transition. While the peak effect is completely absent in $\rho(T)$ data for both films, the behavior of $\rho(H)$ data is significantly different, and seemingly contradictory. In figure 7, $\rho(H)$ data for both films are shown in a semi-log plot to reveal the low resistivity features. The difference between the behavior of the two samples is highlighted in the inset which shows $\rho(H)$ data from both at $T = 4.5$ K normalized to the residual resistivity
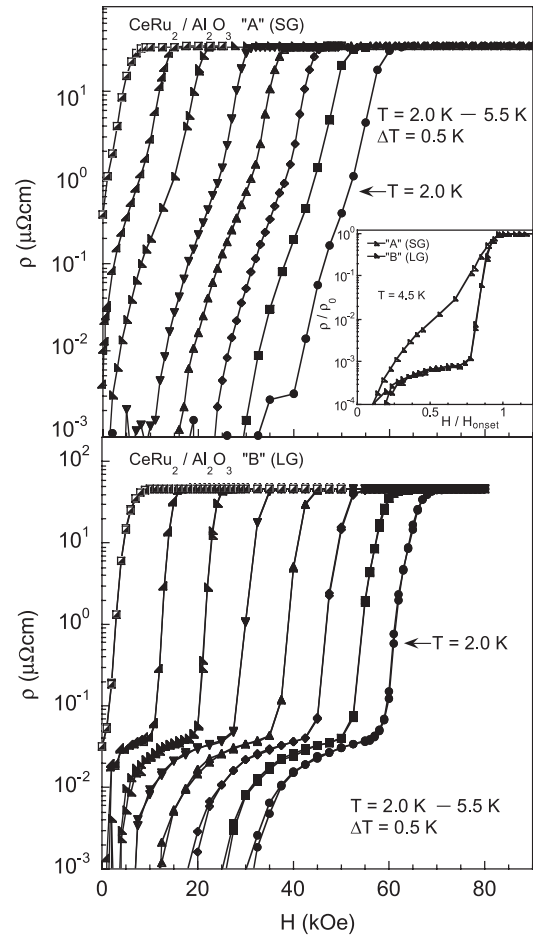
values of ρ_0 and to the onset field, H_{onset}, of the transition. A finite resistivity value is observed down to the lower field value of the peak effect region in both samples. The behavior of the resistivity at field values below H_{onset}, where the peak effect in $\rho(H)$ ought to be seen, can be understood as the result of the extremely weak pinning in these samples, with the higher resistivity contribution from vortex dissipation arising in the cleaner small grain sample. In the inset, note the kink in the data at $H/H_{\mathrm{onset}} \approx 0.7$ for the small grain sample, and the sharp drop in the data at $H/H_{\mathrm{onset}} \approx 0.8$ for the large grain sample. These features are very close to where the resistance would vanish or reach a minimum, if the peak effect were observed [21]. It appears then, from the above results, and also from pinning force calculations presented below, that while the weak pinning condition is definitely satisfied in both samples, this is not a sufficient condition for the peak effect, and thus the peak effect mechanism is frustrated or absent. Furthermore, keeping in mind that all measurements start from the ZFC condition, the complete absence of a resistive signal below the transition in temperature, $\rho(T)$, and the contrasting finite value below the transition in field, $\rho(H)$, points to an obvious difference of the evolution of the
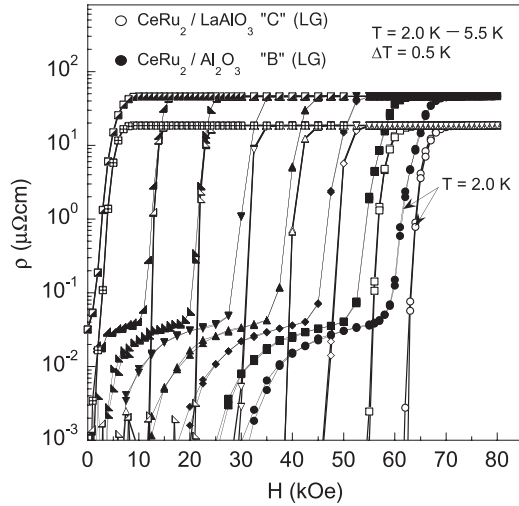
Figure 8. Resistivity, $\rho(H)$, data for film 'C' (LaAlO$_3$ substrate) and film 'B' (Al$_2$O$_3$ substrate), grown at the same time. The different behavior at low fields is attributed to strain in the films. See the text for details.

Figure 9. Critical current density, $J_c(H)$, data of the small grain film 'A' and the large grain film 'B'. The low field J_c values of the two samples are comparable, however, an increase of J_c in the large grain film over that of the small grain film at fields corresponding to the peak effect region is seen.

dynamical state of the vortices upon approaching the transition by increasing either temperature or magnetic field. This difference is further highlighted by the result that the upper critical field lines, determined by using the field/temperature value at a resistivity value of $\rho = 0.1\ \mu\Omega$ cm, $H_{c2}(T)[\rho(H)]$ and $H_{c2}(T)[\rho(T)]$ do not agree and are separated by a distance larger than can be attributed to any experimental error. We suggest the difference in vortex dynamics for the resistive transition in temperature, $\rho(T)$, and in field, $\rho(H)$, as well as the discrepancy between $H_{c2}(T)[\rho(H)]$ and $H_{c2}(T)[\rho(T)]$ can be attributed to differences in the structural response of the atomic lattice with respect to field and temperature. That is, the dynamic behavior of the vortices are responding to changes within their environment, i.e., changes of the electronic band configuration due to thermal or field driven structural deformation and/or fluctuations. Further explanation of this suggestion is given in section 4 below.

Finally, a comparison is made between the behavior of $\rho(H)$ in the large grain film, 'B', and of a similar large grain film grown at the same time, 'C', on a LaAlO$_3$ substrate in figure 8. The samples have a similar morphology (see figure 1 right panel), with slightly larger island diameters on the LaAlO$_3$ grown film, and presumably have the same in-grain point defect density. Remarkably though, in contrast to film 'B', there is no detectable resistive signal in film 'C' in the peak effect region. As seen below, the pinning force density of the LaAlO$_3$ grown sample far exceeds either of the Al$_2$O$_3$ grown films throughout all regions of the phase diagram. With the only difference between the samples being the substrate upon which they were grown, there are two possible explanations for the dramatic difference of pinning characteristics. (i) La ions could conceivably have diffused from the substrate into the the interface region of the CeRu$_2$ film. However, it is unlikely that this would have any impact on the pinning properties since the regions of the film away from the interface would not be contaminated, and it has been shown that La doping produces
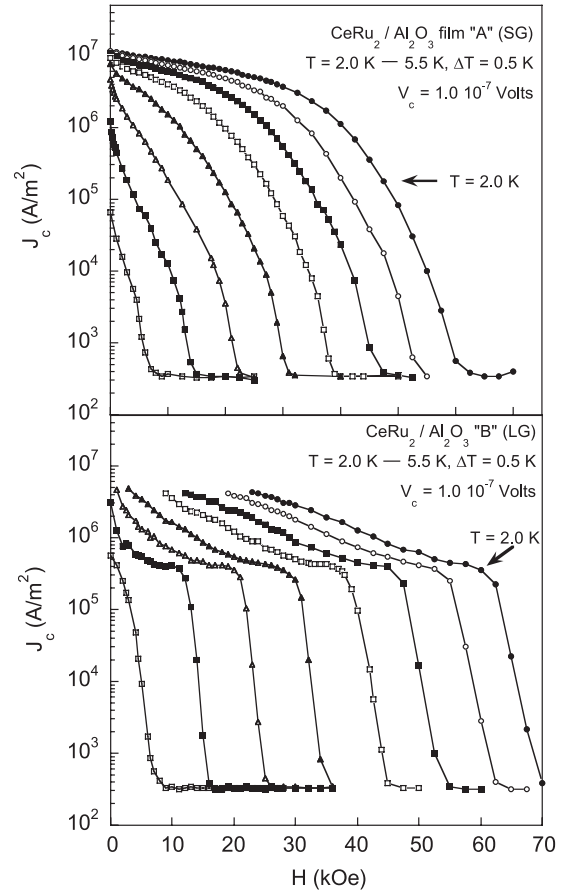
no increase in the pinning potential [22]. (ii) Substrate–film strain is seen to affect the resistivity $\rho(T)$ of the sample as it is cooled down, (as mentioned above for Al$_2$O$_3$ grown sample 'B'), and at low temperatures the strain is the greatest. While the strain distribution throughout the film it is not quantifiable at this time, what is known is that the thermal expansion coefficient values of the substrates are considerably different; 7.50×10^{-6} K^{-1} for Al$_2$O$_3$ and 9.2×10^{-6} K^{-1} for LaAlO$_3$, corresponding approximately to a 20% higher in plane strain on the single crystal islands. How this strain changes the $\rho(H)$ peak effect behavior is a matter we give further attention to in the discussion section below.

We turn attention now to the behavior of the critical current density, $J_c(H, T)$, and pinning force density, $F_p(H, T)$, obtained from V–I measurements, of the small and large grain Al$_2$O$_3$ grown films. The critical current densities, $J_c(H)$, at fixed temperatures, of both samples is shown in figure 9. The value of $J_c(H)$ was determined by the value of the current at a fixed voltage value of 1×10^{-7} V, for each V–I curve. The value of the critical current density in both samples at low fields are nearly equal. In the field regions where the peak effect is expected to occur, we can see a definite increase of the critical current density of the large grain sample over that of the small grain sample.
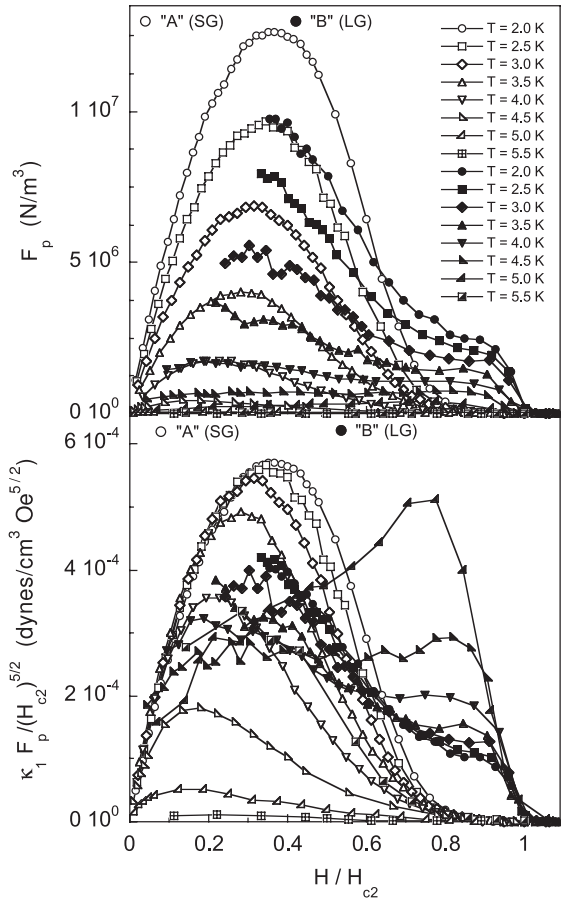
Figure 10. $F_p(H)$ and scaled $F_p(H)$ data for films 'A' and 'B' demonstrating the different behavior in and outside of the peak effect region. Note the emergence of the PE in the *dirtier* film, 'B', similar to that seen in single crystals [23]. A direct comparison of pinning force values of the films to single crystals is complicated by the additional pinning due to grain boundaries in the films.

Figure 11. The enhanced pinning force region of large grain film 'B', corresponding to the peak effect region. Note the double peak structure, as indicated for the $T = 3.5$ K data.

The low field values of J_c, and subsequently F_p, in both films are of the same order of, or less than, that found in high quality single crystals [9, 23]. The pinning force density, defined as $\mathbf{F}_p(H) = \mathbf{J}_c(H) \times \mathbf{H}$, of both samples, at temperatures ranging from 2 to 5 K plotted versus field scaled to the upper critical field, H/H_{c2}, is shown in the top panel of figure 10. The emergence of the peak effect in the large grain sample, already evident from the behavior of the critical current density, is readily seen here. In the lower panel of figure 10, we plot the scaled pinning force, $\kappa_1 F_p/H_{c2}$, as derived by Tenya *et al* [9], where $\kappa_1 = H_{c2}/\sqrt{2}H_c$ is the Ginzburg–Landau parameter. The values of $\kappa_1(T)$ used here to scale F_p are those found by Tenya *et al* [9]. If the pinning mechanism at each temperature value is the same over the entire field range, then $F_p(H)$ will scale onto a single universal curve. The low field–low temperature region of the data of the small grain sample does in fact scale onto a single curve, as does the high field–low temperature region of the data of the large grain sample. It also appears that the low field–low temperature data of the large grain sample might also scale to the same line as the small grain sample, though the data in this region is too limited for a definite observation. These
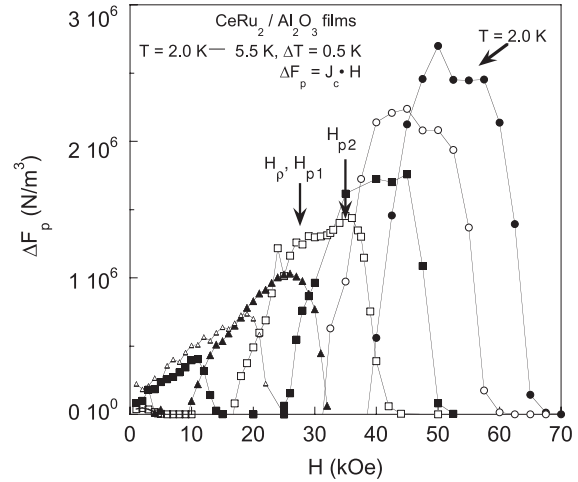
results highlight the different nature of the pinning mechanisms in the conventional and peak effect regions, a result noted for single crystals [23], and a point we will return to in the discussion section below. The difference between the pinning force density, ΔF_p, of the small and large grain samples is shown in figure 11 to further emphasize that the peak effect mechanism is absent in the small grain sample, and that the increase seen in the large grain sample is in fact attributable to the emergence of the peak effect mechanism.

In figure 12 we compare magnetization data from the target sample to that of the large grain film. The peak effect is seen in the target sample and compares to typical results for polycrystalline samples [21]. The magnetization data for the film show that the pinning force density remains finite up to a field value near to the edge of the peak effect region, then collapses to zero. This behavior is observed for all $M(H)$ data at temperatures 5.5 K $\leqslant T \leqslant 6.1$ K. The value of the critical current density, $J_c(H)$, determined via transport measurements, on both films and the difference, $\Delta J_c(H)$, are plotted for comparison. The increase of J_c in the large grain film is seen to be correlated with the peak effect region. Also, indicated by the shaded area, is the region over which the superfluid density is suppressed. This is inferred from scaling of the E–J data discussed below. The important features to be noticed are (i) that the low field boundary of this critical region coincides with the sudden drop in the pinning force density indicated by $M(H)$ data, (ii) the critical field, H_ρ, coincides with the maximum of the peak effect, and (iii) the upper field boundary coincides with the maximum of the pinning force density peak, H_{p2}, inferred from $\Delta F_p(H)$ data, just prior to the collapse of the peak effect region.

We show in the inset of figure 13 electric field versus current density, E–J, data from film 'B', and in the main panel the highlighted portions of the same data after they have been scaled. We have used a modified scaling form based on the model of Fisher *et al* [19], where now the vortex glass correlation length diverges with field as $\xi_g \propto |H - H_g|^{-\nu}$, and E and J scale as $E^* \equiv (E/J)\xi_g^{z+2-d}$ and
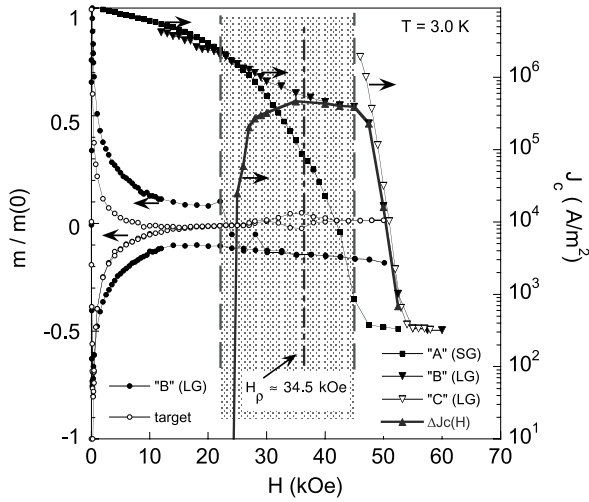
Figure 12. Normalized magnetization data, $M(H)$, at $T = 3.0$ K, for the target sample and the large grain film 'B'. Notice that the peak effect is observable in the polycrystalline target sample, with a region of low to zero critical current density, $J_c = 0$, between the conventional and peak effect regions. The pinning force density of the film remains finite well into the region where it disappears for the target sample, and then rapidly collapses over a small field range at a value just below the peak effect region. Also shown are the critical current densities of the small grain ('A') and large grain films ('B' and 'C') as determined from V–I measurements. Note that the critical current density in film 'C', grown on an $LaAlO_3$ substrate, is much greater than films 'A' and 'B', grown on Al_2O_3 substrates. The difference of the critical current density values of 'A' and 'B', $\Delta J_c(H)$, is plotted as well, emphasizing that the increase of the critical current density, $J_c(H)$, in the large grain sample is attributable to the peak effect. The shaded area corresponds to a region of suppressed superfluid density as evidenced by critical dynamic like vortex behavior with the critical field value, H_g, corresponding to the maximum of the peak effect loop. See the text for further explanation.

$J^* \equiv (J/H)\xi_g^{d-1}$. In appendix A we develop the argument for this form, and show generally that this field dependent scaling of E–J data provides an equivalent description of vortex glass critical dynamic behavior as that of the established temperature dependent scaling form.

We emphasize, however, that the results from using the modified scaling analysis do not correspond to a vortex glass melting transition, i.e., a vanishing linear resistivity of the form $\rho(T) \sim |T - T_g|^{-\nu}$ or $\rho(H) \sim |H - H_g|^{-\nu}$. Thus, we use the notation H_ρ instead of H_g to indicate the critical field about which the data conform to the modified scaling relation of FFH. Recall the above results for $\rho(T)$ where there is no measurable resistivity below the initial, nearly first order, transition. Also, as seen in figure 14, the field value H_ρ lies in the middle of the $\rho(H)$ tail and corresponds to the lower field peak, H_{p1}, of the double peak structure seen in ΔF_p in figure 11, and, the field value of the second peak in ΔF_p corresponds to the usually observed maximum of the anomalous increase of the pinning force density just prior to H_{c2}. Based upon the theoretical arguments developed in appendices A and B, we suggest that the scaling behavior of the E–J data in $CeRu_2$ is evidence of a region of a fluctuating suppression of the superfluid density, ρ_s, centered at H_ρ,
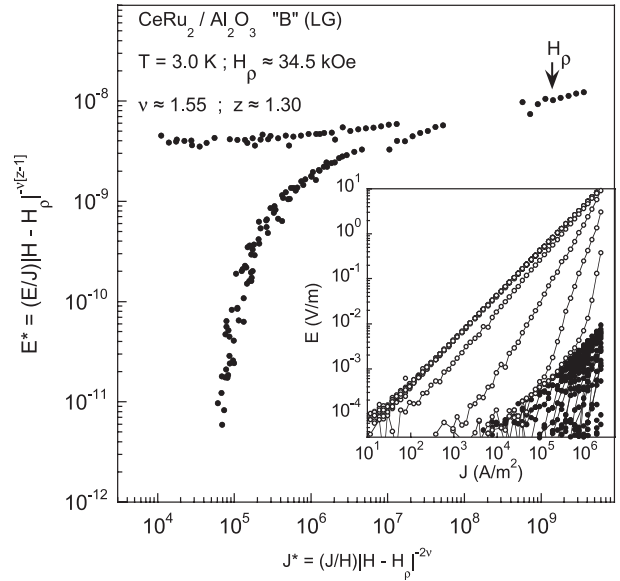

Figure 13. Electric field–current density, E–J, data for the large grain film 'B' scaled by the modified FFH scaling relation given in the text. The inset shows the original E–J data. The data which collapse onto the universal scaling curves shown in the main figure, in the high current density region, are indicated by solid circles. The field H_ρ corresponds to field at which the maximum of the peak effect in $M(H)$ is observed, as shown in figure 12. The range of magnetic field over which the E–J data scale are indicated by the outer edges of the shaded region in figure 12.
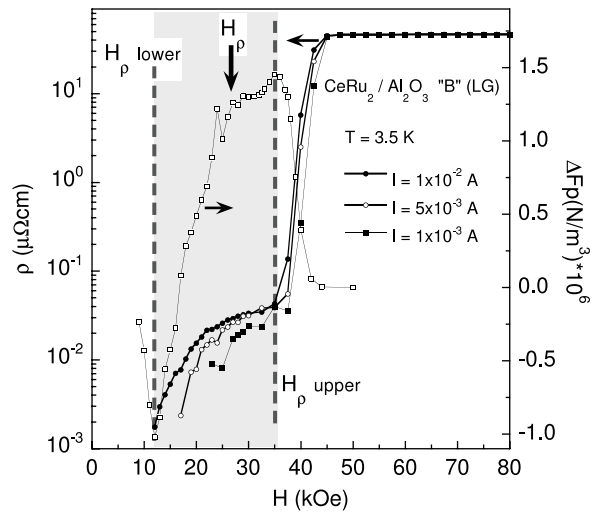
Figure 14. Resistivity, $\rho(H)$, data from the large grain film at various current values. The enhanced pinning force region indicated by $\Delta F_p(H)$, of the film is shown, corresponding to the peak effect region. The field region over which the E–J data scale is indicated by the shaded area, with the critical field H_ρ seen to lie in the middle of the resistive tail.

which coincides with the field value of the maximum of the peak effect magnetization curve, that the fluctuation region as defined by the field values over which E–J scales is the peak effect region, and most importantly that this $H_\rho(T)$ line coincides with at least three other important phenomena known for some time to be associated with the peak effect (figure 15).

Figure 15. Generic behavior of the magnetization, $M(H)$, of a single crystal (solid line, not to scale), and a large grain size film (dashed line). Below 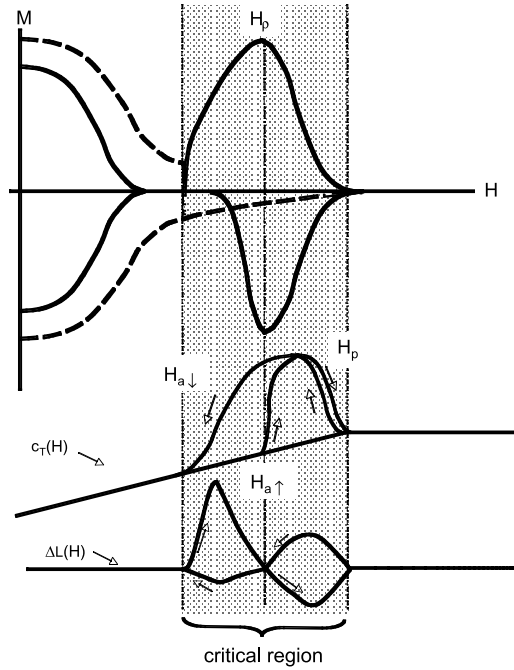is the hysteretic field dependent behavior of the atomic lattice shear moduli, $c_T(H) = \frac{1}{2}(c_{11} - c_{12})(H)$, and the anomalous positive and hysteretic magnetostriction, $\Delta L(H)$.

Figure 16. H–T phase diagram for the large grain CeRu$_2$ film ('B'). The H_{c2} lines determined by $\rho(H)$ and $\rho(T)$ measurements are seen to be significantly separated. The discrepancy between the two lines is larger than experimental error and is attributed to the different effects that increasing temperature or magnetic field have on the vortex dynamics. The $H_\rho(T)$ line, inferred from scaling of E–J data coincides with the $T_{a\uparrow}$ line determined from the shear modulus structural anomaly shown in figure 15. The lines T_c, $T_{a\uparrow}$, and $T_{a\downarrow}$ from Yoshizawa *et al* [8], are scaled in temperature and field to adjust for the different $T_c(0)$ and $H_{c2}(0)$ values of their crystal and of the film. The shaded region indicates the region of scaling of the E–J data corresponding to a suppression of the superfluid density with the minimum density along the H_ρ line.

4. Discussion

Before discussing further the results from our data we first review important results from other studies.

4.1. Review

4.1.1. The softness of CeRu$_2$ and the band structure model. Elastic moduli of high quality CeRu$_2$ single crystals were measured by an ultrasonic method from $T = 300$ to 2 K by Suzuki *et al* [7], and Yoshizawa *et al* [8]. The results of Suzuki *et al* revealed a huge lattice softening in both transverse (c_T) elastic moduli, $(c_{11} - c_{12})/2$ and c_{44}, of 55% and 12%, respectively, over this temperature range, without a structural phase transition. An additional anomaly consisting of a kink at $T = T_c$ in both transverse moduli was also found. The bulk modulus, c_B, however, behaves conventionally, increasing with a decrease of temperature and saturating at low temperature. The shear modulus anomalies and the normal behavior of the bulk modulus are suggestive of structural fluctuations coupling to to the symmetry breaking strain. Based on band structure calculations [24] which reproduce the experimentally determined Fermi surface [25], Suzuki *et al* showed that the unusual elastic behavior can be accounted for by a narrow degenerate band with a high density of states just above E_F which splits in response to the shear strain.

The measurements of $c_T = \frac{1}{2}(c_{11} - c_{12})(H)$ in field by Yoshizawa *et al* revealed even more remarkable anomalous behavior that could be directly correlated with the peak effect. As shown in figure 15, the kink in c_T at $T = T_c$, is suppressed
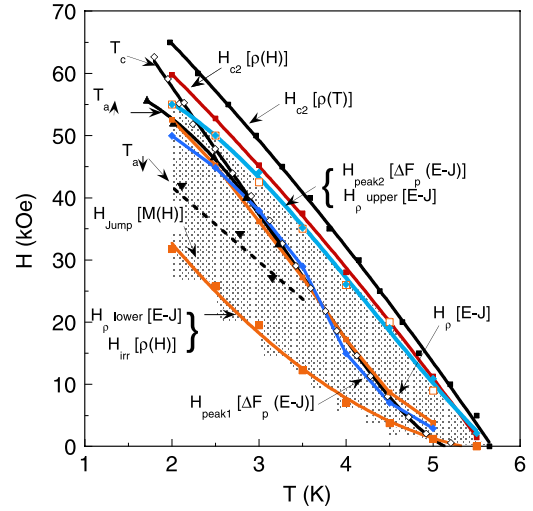
to lower temperatures by a magnetic field, and the field at which this kink occurs corresponds to the upper field of the peak effect region. Additionally, there is an anomalous increase of the value of $c_T(H)$ in the peak effect region *which is hysteretic in a manner that correlates with the hysteresis of the peak effect*, and lies along the same line as the H_ρ line determined from the scaling of E–J data (figure 16).

4.1.2. Relaxation of peak effect region. Time dependent magnetization measurements of CeRu$_2$ in the mixed state by Ho *et al* [10] clearly show a relaxation of the magnetization in the peak effect region. It was observed that the relaxation rate of the magnetization is not uniform over the field loop. Relaxation of the magnetization was seen to occur at a much faster rate in the last quadrant of the loop. This behavior can readily be correlated with the hysteretic features of the magnetization loop and of the transverse elastic moduli c_T. Furthermore, it was found that after a rapid cooling of the sample from room temperature to the superconducting state in zero field, the peak effect was no longer observable. Subsequently, warming the sample back up and cooling at a slow rate resulted in the restoration of the peak effect. This result strongly supports the idea that the structural properties of CeRu$_2$ are a key driving mechanism of the peak effect. The rapid cooling of the sample likely freezes the crystal into a stable, hardened state, a scenario that, as is discussed further below, is possible in materials which undergo a martensitic transformation [26]. This scenario is also consistent with both

the work of Suzuki *et al* [7], mentioned above, wherein a link between band structure properties and the anomalous elastic behavior of the atomic lattice is demonstrated, and of Saini *et al* [27], wherein they find in an x-ray absorption study that band structure effects likely drive the anomalous superconducting behavior of T_c in the $Ce_{1-x}La_xRu_2$ system.

4.1.3. Anomalous magnetostriction behavior.

Tachiki *et al* [4], reported magnetostriction measurements of $CeRu_2$ in the peak effect region. They found an anomalous expansion of the atomic lattice in this region that is hysteretic in field. As shown in figure 15 distinct features of the magnetostriction behavior also correlate with the features of the peak effect. These results have also been considered as evidence for the FFLO state.

While one usually thinks of the pinning force as acting on the vortices, as pointed out by Ikuta *et al* [28, 29], and later by Schleser *et al* an equally large distortion force is transferred to the body of the material [30]. Under normal circumstances the structural integrity of the atomic lattice is such that distortions are a negligible effect. However, as discussed above, due to the weak shear modes at low temperatures, $CeRu_2$ is particularly susceptible to strain forces. There are two stress forces due to the magnetic field to be taken into consideration. (i) that caused by the flux density gradient profile: inward for ascending and outward for descending fields, as described by the critical state model, resulting in dilation or contraction of the crystal along the applied field direction. (ii) the line tension of a vortex flux tube which attempts to restore the flux tube to a straight, (unkinked,) structure. Within the standard London and Ginzburg–Landau theories, there is no coupling between the vortex lattice and the crystal. A full microscopic theory of the mixed state using a nonlocal London model [31] contains this coupling via the nonlocal relation between the current density and the vector potential, $J_\alpha(\mathbf{r}) = \int Q_{\alpha\beta}(\mathbf{r} - \mathbf{r}')A_\beta(\mathbf{r}')\,d^3\mathbf{r}'$, where the kernel Q is dependent upon the Fermi surface, pairing symmetry, and field orientation [32, 33]. Then, if the flux line induced stress is dominant, this would lead to a scenario where, upon entering the peak effect region from the lower field region where the vortex ensemble is a vortex liquid (or in a low pinning state in some cases), a pinning mechanism of a different origin than that in the conventional irreversible region results in an enhanced coupling of the vortices to lattice defects. The restoring force of the vortex line tension results in a contraction (dilation) in the direction perpendicular (parallel) to the field.

4.1.4. Anomalous increase of the penetration depth.

Magnetic penetration depths, λ, in the mixed state of $CeRu_2$, measured by muon spin rotation [12, 13], have been seen to undergo an anomalous increase in the peak effect region. An increase was observed from $\lambda \simeq 2000$ Å at $T = 2$ K in the field region below the peak effect region, to $\bar{\lambda} \simeq 3000$ Å within the peak effect region, indicating a significant fractional increase of the normal state electrons, i.e., quasiparticles, outside of the vortex cores. The maximum of the increase of λ corresponds to the maximum of the peak effect loop. With the penetration depth $\lambda \propto \rho_s^{-1/2}$, and the superfluid density given by [13]

$$\rho_s \propto 1 - N_{env}(H)/N_{env}(H_{c2}), \qquad (2)$$

where $N_{env}(H)$ is the quasiparticle density of states outside of the vortex cores, the above increase of λ corresponds to a reduction of the superfluid density by approximately 50%. This enhancement of the normal state carrier has been shown to be consistent with the generalized FFLO state, where the nodal vortex state results in an increase of the normal state volume of the sample. Below we propose a different explanation as to the origin of the increase of the normal state electrons that is consistent with the experimental results concerning the atomic lattice moduli, c_T and the anomalous magnetostriction behavior discussed above.

4.1.5. The martensitic transformation.

$CeRu_2$ belongs to the C15 cubic Laves phase class of compounds, a structural cousin of the A15 compounds. A structural phase transition known as a martensitic transformation [26], where the lattice undergoes a spontaneous distortion from a cubic to a tetragonal symmetry, is known to occur in superconducting A15 and C15 (Laves phase) compounds [34]. An important characteristic of this class of materials is that a lattice instability will occur at low temperatures if the Fermi energy is close to the bottom of narrow degenerate sub-bands with a high density of states. Near the bottom of these sub-bands the density of states are expected to diverge as $\sim(\epsilon - \epsilon_m^{(0)})^{-1/2}$, where $\epsilon_m^{(0)}$ is the mth sub-band [35]. At temperatures below the transition, T_M, the electrical conductivity increases significantly due to the splitting of the degenerate sub-bands resulting in an excessively high density of states $N(\epsilon_F)$ [35, 36]. Another well know property is that this transition is easily frustrated by disorder [37].

As mentioned above, $CeRu_2$ at low temperatures, is close to, but does not undergo, a structural phase transition. We raise the issue of the martensitic transition for three reasons; (i) this transition is known to occur in the C15 class of compounds to which $CeRu_2$ belongs, (ii) because of the similarity of the electronic band structure arrived at by Suzuki *et al* [7] and that described above, and (iii) an increase of normal state conduction electrons, such as that caused by a martensitic transformation, in the superconducting mixed state would suppress the superfluid density, leading to a softening of the vortex lattice shear modes; providing the mechanism of the peak effect.

An argument against $CeRu_2$ being near a martensitic transformation is that the martensitic transition temperature, T_M, is suppressed to lower temperatures by the application of a magnetic field at a much slower rate than the critical temperature T_c [35, 37], where the shift in temperature is given by

$$\Delta T_M(H) = -0.18T_M(0)[\mu_B H/\epsilon_F(0,0)]^2 \qquad (3)$$

and $\epsilon_F(0,0)$ is the Fermi energy at $T = 0$ in the cubic phase. Since, in the case of $CeRu_2$, at zero field we would have $T_c \gtrsim T_M$, then with the application of a magnetic field T_c would lie below T_M, removing the presumed source of suppression of ρ_s.

While it may be possible that $CeRu_2$ is very close to a martensitic transition that is being frustrated in an unusual manner, this does not need to be the case. What matters is that the degenerate, high density of states band structure of
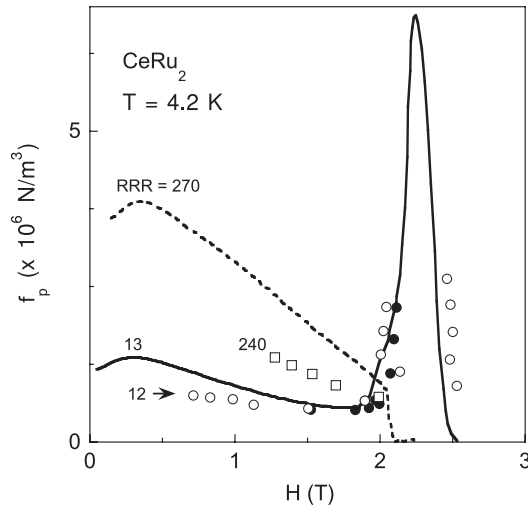
Figure 17. Pinning forces in single crystals of CeRu$_2$, as shown in figure 1 (from Hedo *et al* [23]). The pinning force was determined by current dependent resistivity measurements for the samples with RRR = 12 and RRR = 240, shown by open circles and squares, respectively. Solid circles are obtained from $V–I$ data in fields. Data obtained from magnetization measurements for the RRR = 270 and RRR = 13 samples are shown as dotted and solid lines. Note that for fields below the peak effect region, the pinning force density increases with decreasing disorder, but, in the region of the peak effect the pinning force density disappears for the superclean RRR = 270 sample.

CeRu$_2$ described by Suzuki *et al* [7] will be split in the same manner by the structural fluctuations of the lattice and by the application of a magnetic field.

4.1.6. The missing peak effect in ultraclean CeRu$_2$ single crystals. Shown in figure 17 are the pinning force densities of single crystals of CeRu$_2$ with varying levels of disorder, determined by electrical resistivity measurements, as originally published by Hedo *et al* [23]. These include a superclean sample with a residual resistance ratio (RRR) of 270, a very clean (RRR = 240), and dirty (RRR = 13) crystal. Remarkably, the pinning force density disappears in the peak effect region in the superclean crystal. A similar result was seen by Tenya *et al* [38], where they observe that the peak effect from $M(H)$ becomes weaker with increasing RRR. It appears then that disorder is actually a necessary ingredient for the peak effect mechanism, a point we will return to below.

4.2. Current results: relation to known peak effect anomalies

The question naturally arises as to why the peak effect is completely absent in the small grain film, and only emergent in the large grain film, if they are of such high quality with respect to lattice defects within the grains. We develop below an argument for what this result, along with the evidence for suppression of the superfluid density from the scaling analysis of the $E–J$ data, contributes to the picture of the peak effect mechanism in CeRu$_2$.

The evidence from the studies reviewed above strongly point to a structural-electronic origin of the peak effect. The simple explanation for the results of this study is that the grains of the films are under differing average levels of strain. The small grains of film 'A' have a higher level of surface tension, and smaller available internal volume able to undergo the intrinsic atomic lattice deformation process. The large grains of film 'C', grown on the LaAlO$_3$ substrate, are well attached to the substrate and experiences a larger interface strain than film 'B', grown on an Al$_2$O$_3$ substrate. Film 'B', under the least external and surface strain, exhibits a nascent peak effect because it is able to deform just enough to begin the structure driven splitting of the degenerate electronic sub-band and shifting of energy levels.

While this explanation of the 'missing' peak effect in our films is consistent, there remains the matter of the 'missing' peak effect observed in ultraclean CeRu$_2$ single crystals [23, 9], mentioned above. Since the crystals in the above studies are relatively large and of the same size, then the size/strain effect postulated for the grains cannot be relevant here. Thus, disorder to a certain extent plays a role in enhancing or aiding the peak effect process. We consider two possible reasons for this. (i) As happens with the martensitic transformation discussed above, the structural deformation process is likely readily frustrated by defects. The deformation of the atomic lattice is tied to the electronic properties, i.e., the band splitting effects. If the deformation is unimpeded and the splitting of the bands continues beyond a critical level, then $N(\epsilon_F)$ will be excessively large and the superfluid density will never recover enough stiffness to allow the vortex lattice to acquire a sufficiently strong shear modulus, thus the enhancement of the ability of the vortices to acquire a higher pinning configuration will be lost to the over weakening of the rigidity of the vortex lattice. (ii) The coupling of the vortices to the lattice plays an important role in driving or sustaining the peak effect mechanism. (a) The absence of defects removes the defect-vortex line coupling strain from the deformation dynamics. A nearly perfect vortex lattice, with its motion unimpeded will be easily displaced by the Lorentz force of an applied current, resulting in transport behavior of the TAFF kind, as observed in the small grain film whose grain dimensions are of the same length scale as the mean free path. (b) The collective critical nature of the vortices indicated by the scaling of the $E–J$ data may provide an enhancement of the vortex line tension via the correlated dynamical manner in which vortex motion takes place, beyond that of the single line picture.

While the point in (i) above sufficiently explains the single crystal picture, and it is not invalidated by the results from the films, it cannot be the case here if, as presumed, the strained state of the films prevents the initiation of the peak effect mechanism. Thus, we explore the latter idea further, particularly the collective nature of the vortices in the peak effect region.

If, as suggested by the scaling properties of the $E–J$ data in the large grain sample, the vortex ensemble is in a critical dynamical state akin to a vortex glass critical region, then a correlation length scale, ξ^{vg}, associated with the dynamical behavior plays a relevant physical role. Using the scaled $E–J$ data from the large grain sample, we calculate the coherence length of the vortex glass at the boundary of the peak effect

Table 1. Values of the critical temperature, T_g, and field, H_g for the large grain film. Also listed are values for the zero temperature vortex glass correlation length ξ_0^{vg}, the values of ξ^{vg} and the lattice constant a_Δ at the lower field of the peak effect region, ξ_-^{vg} and a_Δ^-, respectively, and the ratio of the temperature at which the correlation length will exceed the grain size to the temperature at the critical line, $H_g(T)$, for the small and large grain films.

T (K)	H_g (T)	ξ_0^{vg} (Å)	$\Delta\xi_0^{vg}$ (Å)	ξ_-^{vg} (Å)	a_Δ^- (Å)	t_{sg}	t_{lg}
2.0	5.25	180	65	1 160	271	0.75	0.94
2.5	4.52	320	105	2 300	309	0.61	0.91
3.0	3.62	1100	240	9 240	346	0.05	0.78
3.5	2.72	1580	370	27 800	489	—	0.56
4.0	1.72	1670	460	41 900	631	—	0.43
4.5	0.87	1900	690	87 610	892	—	0.08

region [19, 39]. The values are given in table 1. It is seen that the coherence length, ξ^{vg} is effectively cutoff by the grain size dimensions in the small grain film prior to, or just inside the peak effect region, and will be cutoff at some point in the peak effect region prior to the critical field line H_ρ. While these results are certainly not conclusive, they suggest that the granular regions must reach a critical size to support the critical dynamic vortex behavior, which in turn, plays a supporting role in the structural deformation process of the atomic lattice. The enhancement of vortex line–atomic lattice coupling in the peak effect region may not require the somewhat exotic scenario suggested above, but it is apparent that a sufficient amount of disorder must be present for the vortices to be able to couple to, and exert strain upon, the atomic lattice. What should be understood from the scaling of the E–J data, is that the dynamic properties of the vortices are changing in response to a change in their environment, and as such, the $H_\rho(T)$ line does not necessarily constitute a vortex phase transition boundary.

Finally, we are left then with the following scenario summary: the peak effect occurs because of enhanced pinning of the vortices. The enhanced pinning is a result of the vortices being able to rearrange into a stronger (more tangled) pinning configuration. This is made possible by a weakening of the shear moduli of the vortex lattice. The weakening of the vortex lattice shear moduli is a result of a reduction of the superfluid density, $c_{66} \propto \rho_s$, etc. The suppression of the superfluid density comes from an increase of the normal state electrons, quasiparticles, outside of the vortex core. The increase of quasiparticles has two possible (and not mutually exclusive) sources. (i) The GFFLO state described above. (ii) A frustrated martensitic like scenario which is consistent with both the observed lattice softening in CeRu$_2$ and the doubly degenerate band model of Suzuki *et al* [7].

The latter scenario is the interpretation we favor. Many previous arguments against the GFFLO state persist. Additionally, the difference in the upper critical field lines, $H_{c2}(T)$, determined by resitivity data as a function of field or temperature, $H_{c2}(T)[\rho(H)]$ or $H_{c2}(T)[\rho(T)]$, reveals an asymmetry of the vortex dynamical state with respect to approaching the upper critical field in temperature or magnetic field. This asymmetry is not accounted for by the (G)FFLO model, but can be attributed to a field–temperature asymmetry of the strain moduli. The anomalous increase of the normal state electron density in the peak effect region can be explained naturally by a band structure that is known to exist. The

lattice deformation-electronic band splitting phenomenon may be frustrated or aided by magnetostriction effects. If this is the case, this could possibly be investigated by measurements of the superfluid density in single crystals with a variation of the angular dependence of the applied field, or by measurements under uniaxial and/or hydrostatic pressure.

5. Summary

We report the first study of the peak effect in CeRu$_2$ films grown by the pulsed laser ablation method. We have investigated the peak effect via electrical transport, $\rho(H, T)$, critical current density, $J_c(H, T)$, and magnetization, $M(H, T)$ measurements. The pinning force density, determined by transport measurements, in the peak effect region *is nearly zero* in the small grain film, and is seen to be emerging with a much lower than usual strength in the large grain size film. Magnetization, $M(H)$, measurements indicate a zero pinning force density in both samples in the peak effect region. In the region of the emerging peak effect, the large grain film exhibits electrical transport behavior reminiscent of the dynamical behavior of a vortex glass. In this same region, transport measurements of the small grain size film are found to be consistent with a thermally assisted flux flow (TAFF) scenario. The vortex glass like behavior associated with the peak effect in the large grain film is considered to be evidence of fluctuations of the superfluid density, ρ_s. We find evidence for an important role of the softening of the atomic lattice moduli, from previous ultrasound, magnetostriction, and magnetic relaxation studies [7, 8, 4, 10], and for the coupling of the vortex lattice to the atomic lattice. The critical behavior of vortices in the large grain film, inferred from scaled E–J data, can be correlated with both the anomalous field dependence of the shear moduli and the magnetostriction.

Our study strongly suggests the origin of the peak effect in CeRu$_2$ has a conventional explanation, originating with the unusual structural properties and the degenerate band structure near the Fermi level.

Appendix A. Modified vortex glass scaling model

The current–voltage characteristics of a vortex ensemble that undergoes a vortex glass melting transition in a fixed magnetic field, H, is such that, as the temperature approaches the transition temperature T_g, E–J data will scale according to the form arrived at from the ansatz of Fisher, Fisher, and Huse (FFH) [17, 19]. The dissipative electric field with a dc current density J will scale as

$$E \approx J\xi_g^{d-2-z}\mathcal{E}_\pm(J\phi_0\xi^{d-1}/cT) \qquad (A.1)$$

from which the scaled electric field and current densities are then given by $E^* \equiv (E/J)\xi_g^{z+2-d}$ and $J^* \equiv (J/T)\xi_g^{d-1}$. ξ_g is the vortex glass coherence length which in the critical melting region vanishes linearly with temperature such that $\xi_g \propto |T - T_g|^{-\nu}$. The exponents ν and z are referred to as the static and dynamical critical exponents, and d is the dimensionality of the vortex system.

Starting from the form of the coherence length given by Brandt [40], $\xi_g(H, T) = \xi_g(H)|1 - T/T_g|^{-\nu}$, we would naturally expect a divergence of the correlation length scale $\xi_g(H, T)$ regardless of whether the melting line is approached in field or temperature. The assumption that $\xi_g(H)$ should take the form $\xi_g(H) \propto |1 - H/H_g|^{-\nu}$ is supported by both experimental observation and related theoretical models. Electrical transport data exhibit a linear dependence with respect to field, H, over a range beginning at a critical field H_g when plotted as $[d[\ln\rho]/dH]^{-1}$ versus H. This field dependence is analogous to the linear temperature dependence of $\rho(T)$ data plotted as $[d[\ln\rho]/dT]^{-1}$ versus T over a temperature range beginning at the critical temperature T_g and extending up to a temperature T_g^u corresponding to the upper limit of the critical region. Theoretical support for this form can be found both in the work of Gingras and Huse [41], and Fisher [18]. In the former, is it observed, within the context of the random field X–Y model with topological defects, that the correlation length ξ diverges as $\xi \sim (H - H_c)^{-\nu}$ as a transition from a topologically ordered phase to a disordered phase is approached. Fisher considered the scenario when the field-tuned superconductor–insulator transition from the vortex to electron glass phase is approached as the magnetic field increases in the $T \rightarrow 0$ limit. The assumption was also made that as one nears the critical field of the transition, B_c, a diverging correlation length is expected such that $\xi_B \sim (B - B_c)^{-\nu}$.

Next, we return to the derivation for the original expression for the scaling form of the current density arrived at by FFH [19], $J^* \equiv (J/T)\xi_g^{d-1}$. This expression is found by the argument that the characteristic current density within the scaling regime will be that which is large enough to change the statistics of the phase of the order parameter and that of the vortex line fluctuations. In an isotropic system, the variation in the phase will be $\sim 2\pi$ within a correlation volume so then $|\nabla\phi| \sim 1/\xi$. With the coupling of an external current to a phase gradient via

$$\delta F_J = -\int \frac{\phi_0}{c}\mathbf{J} \cdot \nabla\phi, \qquad (A.2)$$

then, within a correlation volume ξ^D, δF_J will be of the order of k_BT, and thus of similar magnitude to the spontaneous fluctuations when $J \sim (cT)/\phi_0\xi^{d-1}$ (where c is a constant). However, from the perspective of approaching the critical region by an increase in field at a fixed temperature, the increase of the free energy of the superfluid density is proportional to the number of flux lines within the superfluid, which is proportional to the applied magnetic field H. Then, within the same correlation volume ξ^D, we will have $\delta F_J \sim H$ and comparable in magnitude to the spontaneous fluctuations when $J \sim (cH)/\phi_0\xi^{d-1}$ (where c is a different constant than above). Hence, it follows, that as the critical region is approached in the H–T phase diagram along the field axis we expect similar scaling properties as those established by FFH, with now E and J scaling as $E^* \equiv (E/J)|H - H_g|^{-\nu(z+2-d)}$ and $J^* \equiv (J/H)|H - H_g|^{-\nu(d-1)}$.

Appendix B. Critical behavior: suppression of the superfluid density

Here we show that the scaling forms of E^*–J^* as given by FFH [19] or those derived in appendix A, give information about the superfluid density ρ_s in the critical region.

For simplicity, we work with the scaling forms given by FFH [19]. From the form of the complex conductivity at low frequency and $T < T_c$,

$$\sigma(\omega) \approx \rho_s/(-i\omega + \epsilon) \qquad (B.1)$$

and, using the scaling properties in the critical region where the relaxation timescales as $\tau \sim \xi^z$ [19], the superfluid density scales as $\rho_s \sim \xi^{2-d}$ [19, 42], with $\xi \sim |T - T_c|^{-\nu}$, the scaling relation of the frequency dependent conductivity is then

$$\sigma(\omega) \approx \xi^{z+2-d}\mathcal{S}_\pm(\omega\xi^z). \qquad (B.2)$$

When $T \rightarrow T_c^+$, the dc conductivity, $\sigma(0)$, diverges as $\tau\rho_s \sim \xi^{z+2-d}$.

The FFH ansatz generalizes the zero field scaling properties of the superconducting transition to the vortex glass melting transition, where the melting line is considered to be a line of critical points so that $T_c \Rightarrow T_g$, and $\xi_g \sim |T - T_g|^{-\nu}$.

Then, by using the relation $J = \sigma E$ and the in-field scaling of the conductivity given by FFH, it follows that

$$\frac{J}{E}\xi_g^{-(z+2-d)} \sim \tau\rho_s. \qquad (B.3)$$

References

[1] Matthias B T, Suhl H and Corenzwit E 1958 *Phys. Rev. Lett.* **1** 449
[2] Fulde P and Ferrell R A 1964 *Phys. Rev.* **135** A550
[3] Larkin A I and Ovchinnikov Yu N 1965 *Sov. Phys.—JTEP* **20** 762
[4] Tachiki M, Takahashi S, Gegenwart P, Weiden M, Lang M, Geibel C, Steglich F, Modler R, Paulsen C and Ônuki Y 1966 *Z. Phys.* B **100** 369
[5] Dilley N R and Maple M B 1997 *Physica* C **278** 207
[6] Kadowaki K, Takeya H and Hirata K 1996 *Phys. Rev.* B **54** 462

[7] Suzuki T, Goshimia H, Sakita S, Fujita T, Hedo M, Inada Y, Yamamoto E, Haga Y and Ônuki Y 1996 *J. Phys. Soc. Japan* **65** 2753

[8] Yoshizawa M, Tamura M, Ozawa M, Yoon D-H, Sugawara H, Sato H and Ônuki Y 1997 *J. Phys. Soc. Japan* **66** 2355

[9] Tenya K, Yasunami S, Tayama T, Amitsuka H, Sakakibara T, Hedo M, Inada Y, Yamamoto E, Haga Y and Ônuki Y 1999 *J. Phys. Soc. Japan* **68** 224

[10] Ho P-C, Moehlecke S and Maple M B 2005 *Preprint* cond-mat/0301281

[11] Groten D, Ramakrishnan S, Becker B, Nieuwenhuys G J, Mydosh J A and Aarts J 1997 *Physica* B **230** 377

[12] Yamashita A, Ishii K, Yokoo T, Akimitsu J, Hedo M, Inada Y, Ônuki Y, Yamamoto E, Haga Y and Kadono R 1997 *Phys. Rev. Lett.* **79** 3771

[13] Kadono R, Higemoto W, Koda A, Ohishi K, Yokoo T, Akimitsu J, Hedo M, Inada Y, Ônuki Y, Yamamoto E and Haga Y 2001 *Phys. Rev.* B **63** 224520

[14] Cronemeyer D C 1991 *J. Appl. Phys.* **70** 2911

[15] Inada Y and Ônuki Y 1999 *Low Temp. Phys.* **25** 573

[16] Orlando T P and Beasley M R 1981 *Phys. Rev. Lett.* **46** 1598

[17] Fisher M P A 1989 *Phys. Rev. Lett.* **62** 1415

[18] Fisher M P A 1990 *Phys. Rev. Lett.* **65** 923

[19] Fisher D S, Fisher M P A and Huse D A 1991 *Phys. Rev.* B **43** 130

[20] Giamarchi T and Le Doussal P 1995 *Phys. Rev.* B **52** 1242
Giamarchi T and Le Doussal P 1997 *Phys. Rev.* B **55** 6577

[21] Dilley N R, Herrmann J, Han S H, Maple M B, Spagna S, Diederichs J and Sager R E 1996 *Physica* C **265** 150

[22] Groten D, Ardonne E, Ramakrishnan S, Nieuwenhuys G J and Mydosh J A 1998 *Physica* C **306** 271

[23] Hedo M *et al* 1999 *Physica* B **259** 688

[24] Higuchi M and Hasegawa A 1996 *J. Phys. Soc. Japan* **65** 1302

[25] Hedo M, Inada Y, Ishida T, Yamamoto E, Haga Y, Ônuki Y, Higuchi M and Hasegawa A 1995 *J. Phys. Soc. Japan* **64** 4535

[26] Callister W D Jr 1985 *Materials Science and Engineering, an Introduction* (New York: Wiley)

[27] Saini N L, Agrestini S, Amato E, Filippi M, Di Castro D, Bianconi A, Manfrinetti P, Palenzona A and Marcelli A 2004 *Phys. Rev.* B **70** 094509

[28] Ikuta H, Hirota N, Nakayama Y, Kishio K and Kitazawa K 1993 *Phys. Rev. Lett.* **70** 2166

[29] Ikuta H, Kishio K and Kitazawa K 1994 *J. Appl. Phys.* **76** 4776

[30] Schleser R, van der Linden P J E M, Wyder P and Gerber A 2003 *Phys. Rev.* B **67** 134516

[31] Kogan V G, Gurevich A, Cho J H, Johnston D C, Xu M, Thompson J R and Martynovich A 1996 *Phys. Rev.* B **54** 12386
Kogan V G, Bullock M, Harmon B, Miranovic P, Dobrosavljevic-Grujic Lj, Gammel P L and Bishop D J 1997 *Phys. Rev.* B **55** R8693

[32] Gurevich A and Kogan V G 2001 *Phys. Rev. Lett.* **87** 177009

[33] Miranović P and Kogan V G 2001 *Phys. Rev. Lett.* **87** 137002

[34] Pushin V G and Kondrat'ev V V 1994 *Fiz. Met. Metalloved.* **78** 40

[35] Maita J P and Bucher E 1972 *Phys. Rev. Lett.* **29** 931

[36] Ikeda K, Gschneidner K A Jr, Beaudry B J and Ito T 1982 *Phys. Rev.* B **25** 4618
Ikeda K, Gschneidner K A Jr, Beaudry B J and Atzmony U 1982 *Phys. Rev.* B **25** 4604

[37] Šebek J, Mihalik M, Syshchenko O and Vejpravová J 2002 *Czech. J. Phys.* **52** 291

[38] Tenya K, Yasunami S, Tayama T, Amitsuka H, Sakakibara T, Hedo M, Inada Y, Haga Y, Yamamoto E and Ônuki Y 1999 *Physica* B **259** 692

[39] Li S, Taylor B J, Frederick N A, Maple M B, Nesterenko V F and Indrakanti S S 2002 *Physica* C **382** 177

[40] Brandt E H 1995 *Rep. Prog. Phys.* **58** 1465

[41] Gingras M J P and Huse D A 1996 *Phys. Rev.* B **53** 15193

[42] Fisher M E, Barber M N and Jasnow D 1973 *Phys. Rev.* A **8** 1111